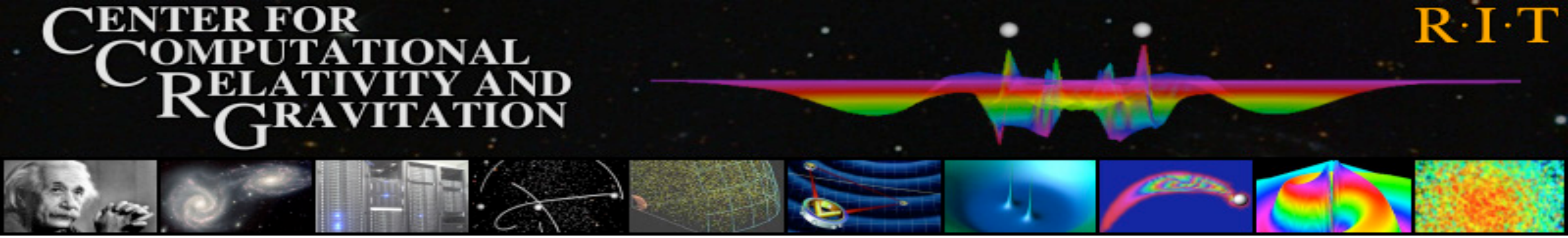

Session 8: Modeling Challenges

Carlos Lousto, Rochester Institute of Technology

PAX meeting, Pisa, Italy, May 27-29th, 2019

LIGO-P1800300

Overview

1. *NR Waveforms Catalogs:* Applications to GW direct and complete binary parameter estimations.
2. *Precessing dynamics*: Flip-flops, alignment instability, GW Beacons.
3. Discussion: Getting ready for GW next detections: Highly spinning BBH, small mass ratios, BHNS. Pulsar Timing. LISA.

RIT BBH Waveform Catalog

- 2nd release of the BBH public RIT catalog at http://ccrg.rit.edu/~RITCatalog.html
- 320 waveforms:

  274 nonprecessing + 46 precessing
- $1/6 \leq q \leq 1, \ \frac{s}{m^2} \leq 0.95, \ \ell \leq 4$

Aligned Cases:

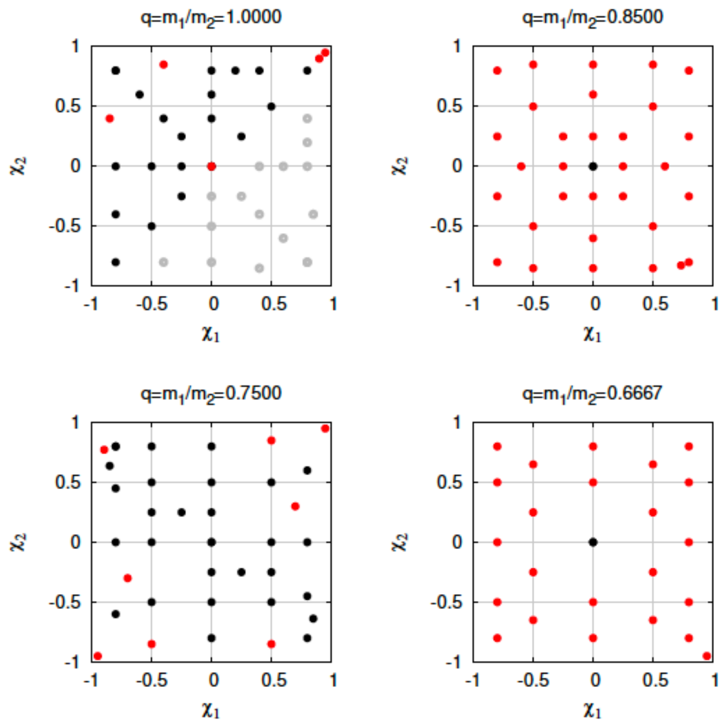

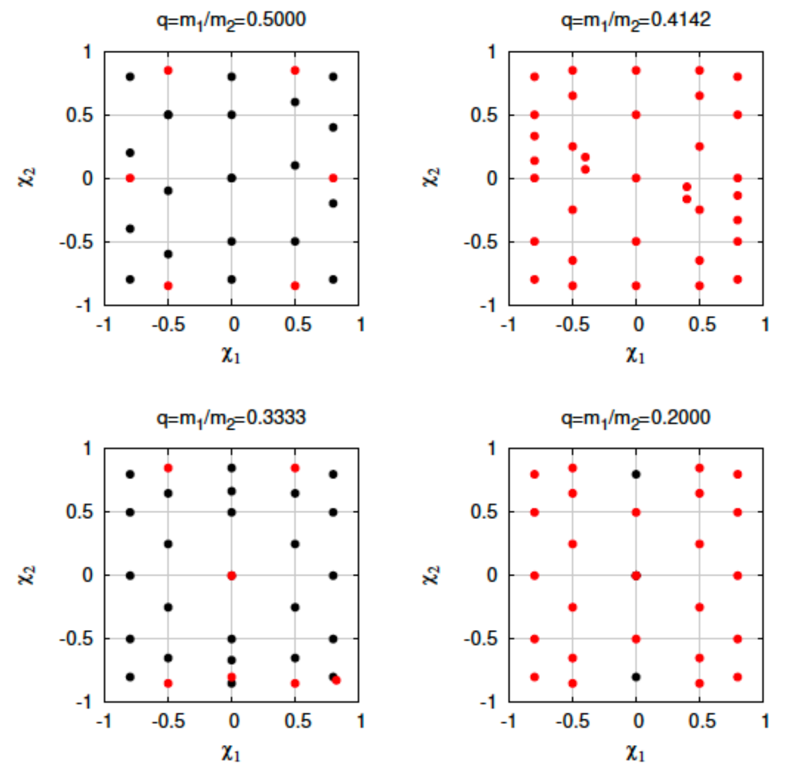

FIG. 1. Initial parameters in the (q, χ_1, χ_2) space for the 274 nonprecessing binaries. Note that χ_i denotes the component of the dimensionless spin of BH i along the orbital angular momentum. Each panel corresponds to a given mass ratio that covers the comparable masses binary range from $q = 1$ to $q = 1/5$. The dots in black denote the simulations of the catalog first release, and the dots in red are those of this second release.

From: Healy et al. arXiv:1901.02553 [gr-qc]

GW150914: Heat Maps

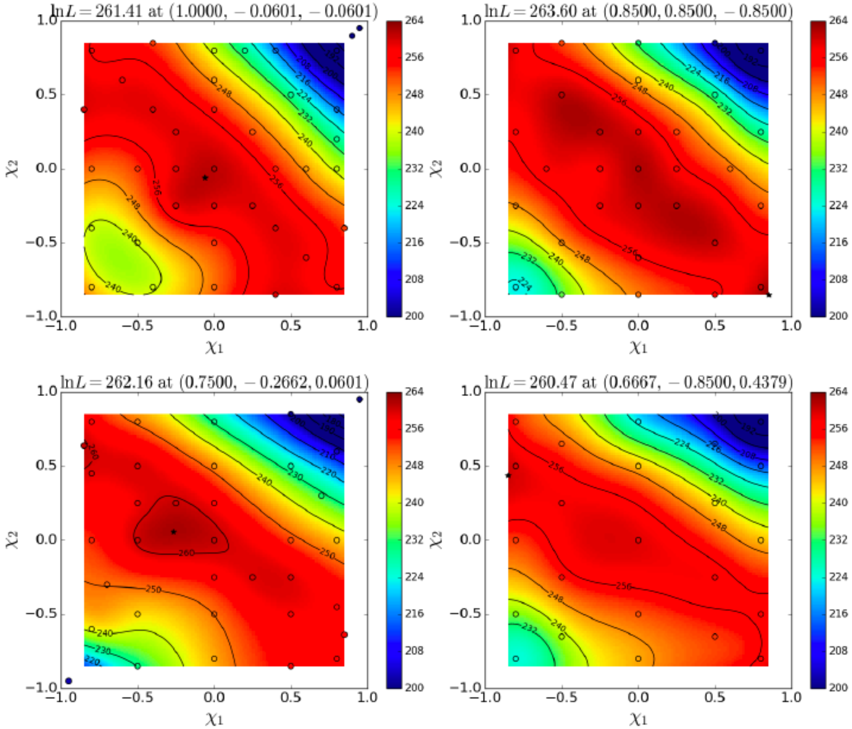

$$\ln \mathcal{L}(\boldsymbol{\lambda};\theta) = -\frac{1}{2}\sum_k \langle h_k(\boldsymbol{\lambda},\theta) - d_k | h_k(\boldsymbol{\lambda},\theta) - d_k\rangle_k - \langle d_k|d_k\rangle_k, \tag{1}$$

where h_k are the predicted response of the kth detector due to a source with parameters ($\boldsymbol{\lambda}$, θ) and d_k are the detector data in each instrument k; $\boldsymbol{\lambda}$ denotes the combination of redshifted mass M_z and the remaining intrinsic parameters (mass ratio and spins; with eccentricity ≈ 0) needed to uniquely specify the binary's dynamics; θ represents the seven extrinsic parameters (4 spacetime coordinates for the coalescence event and 3 Euler angles for the binary's orientation relative to the Earth); and $\langle a|b\rangle_k \equiv \int_{-\infty}^{\infty} 2df \tilde{a}(f)^* \tilde{b}(f)/S_{h,k}(|f|)$ is an inner product implied by the kth detector's noise power spectrum $S_{h,k}(f)$. In practice we adopt a low-frequency cutoff $f_{\rm min}$ so all inner products are modified to

$$\langle a|b\rangle_k \equiv 2\int_{|f|>f_{\rm min}} df \frac{[\tilde{a}(f)]^*\tilde{b}(f)}{S_{h,k}(|f|)}. \tag{2}$$

The 90% confidence level gives

$$\begin{aligned} 0.570 &< q < 1.00, \\ 0.00 &< |\chi_1| < 1.00, \\ 0.00 &< |\chi_2| < 0.78, \\ -0.44 &< \chi_{\rm eff} < 0.14, \\ -0.44 &< S_{hu} < 0.14, \\ 66.3 &< M_{total} < 79.2 \end{aligned}$$

Compare these values to the GW150914 properties

$$\begin{aligned} 0.62 &< q < 0.99, \\ 0.04 &< |\chi_1| < 0.90, \\ 0.03 &< |\chi_2| < 0.78, \\ -0.29 &< \chi_{\rm eff} < 0.1, \\ 66.1 &< M_{total} < 75.2 \end{aligned}$$

Where M_{total} is given in solar mass $M_\odot$ units.

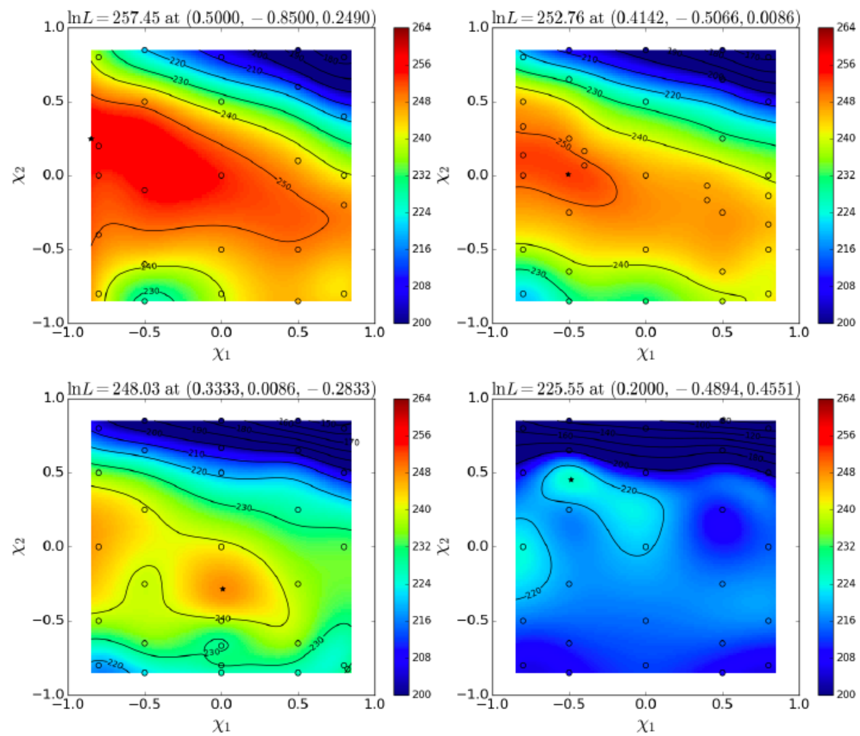

FIG. 4. Heat maps of the GW150914 likelihood for each of the eight mass ratio panels covering form $q = 1$ to $q = 1/5$ and aligned/antialigned individual spins. The individual panel with $q = 0.85$ contains the highest likelihood. Contour lines are in increments of 5. The interpolated $\ln \mathcal{L}$ maximum at its location in (q, χ_1, χ_2) space is given in each panel's title and denoted by the * in the plots.

Effective Spin variables

Fig. 6 displays a comparative analysis of the single spin approximations to aligned binaries using a linear interpolation. The upper panel presents our preferred variables for the spin, S_{hu}

$$m^2\,S_{hu} = \left((1+\frac{1}{2q})\,\vec{S}_1 + (1+\frac{1}{2}q)\,\vec{S}_2\right)\cdot\hat{L}, \qquad (3)$$

to describe the leading effect of hangup on the waveforms [30]. The lower panel displays a comparative heatmap using the common approximate model variable [97]

$$m^2\,\chi_{eff} = \left((1+\frac{1}{q})\,\vec{S}_1 + (1+q)\,\vec{S}_2\right)\cdot\hat{L}.$$

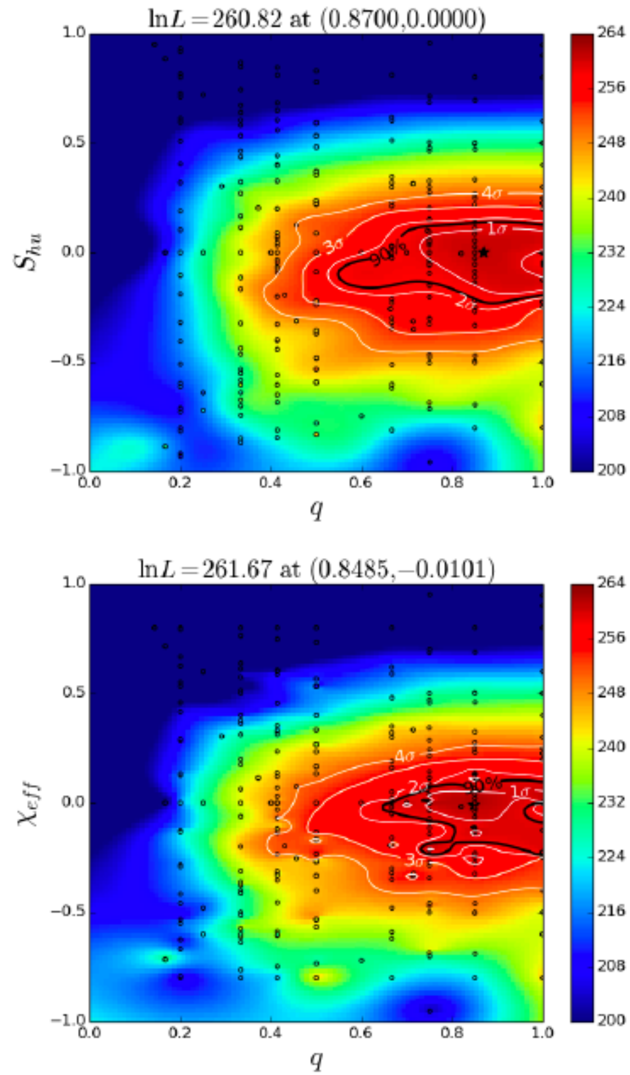

FIG. 6. Heat maps of the GW150914 likelihood for the aligned binary with effective variables S_{hu} and χ_{eff} versus mass ratios using linear interpolation. In black the 90% confidence contours and the interpolated $\ln\mathcal{L}$ maximum is given in each panel's title and denoted by the * in the plots.

The latter exhibits some "pinch" points around some simulations suggesting a remaining degeneracy by using χ_{eff}. Such features are not seen using the (normalized) variable S_{hu}, which represents a better fitting to waveform phases as shown in [30], suggesting again that it is a better (or at least a valid alternative) choice to describe aligned binaries.

[30] J. Healy and C. O. Lousto, Phys. Rev. **D97**, 084002 (2018), arXiv:1801.08162 [gr-qc].

S_{hu} perhaps a better spin variable for waveform modeling

Hangup revisited: Unequal masses

We will study the hangup dependence of those 181 simulations on the variable

$$\frac{1}{1-C}S_{\rm hu} = (\vec{S}\cdot\hat{L} + C\delta m\vec{\Delta}\cdot\hat{L}), \qquad (10)$$

where C will be the fitting parameter that regulates the coupling to the total spin $\vec{S}$ with the "delta" combination $\delta m\vec{\Delta}$.

$$\eta[N - N_0] = D + AS_{\rm hu} + BS_{\rm hu}^2, \qquad (11)$$

are presented in Fig. 2. This shows the dependence of the hangup effect with respect to the nonspinning binaries. We see that this dependence can be expressed in terms of the spin variable

$$\frac{3}{2}S_{\rm hu} = \left(\vec{S}\cdot\hat{L} + \frac{1}{3}\delta m\vec{\Delta}\cdot\hat{L}\right), \qquad (12)$$

to an excellent degree of approximation since $C = 0.3347$ from the fits.

TABLE I. RMS and variance of S_0, $S_{\rm eff}$, and $S_{\rm hu}$ fits. Here we show ndf (no. degrees of freedom), WSSR = weighted sum of the residuals, $\mathrm{RMS} = \sqrt{\mathrm{WSSR/ndf}}$, and Variance = reduced χ^2 = WSSR/ndf.

Variable	Coefficient	ndf	WSSR	RMS	Variance
S_0	0.5	167	0.702	0.065	0.0042
$S_{\rm eff}$	0.428571	167	0.361	0.047	0.0022
$S_{\rm PN}$	0.398936	167	0.281	0.041	0.0017
$S_{\rm hu}$	0.333333	167	0.214	0.036	0.0013

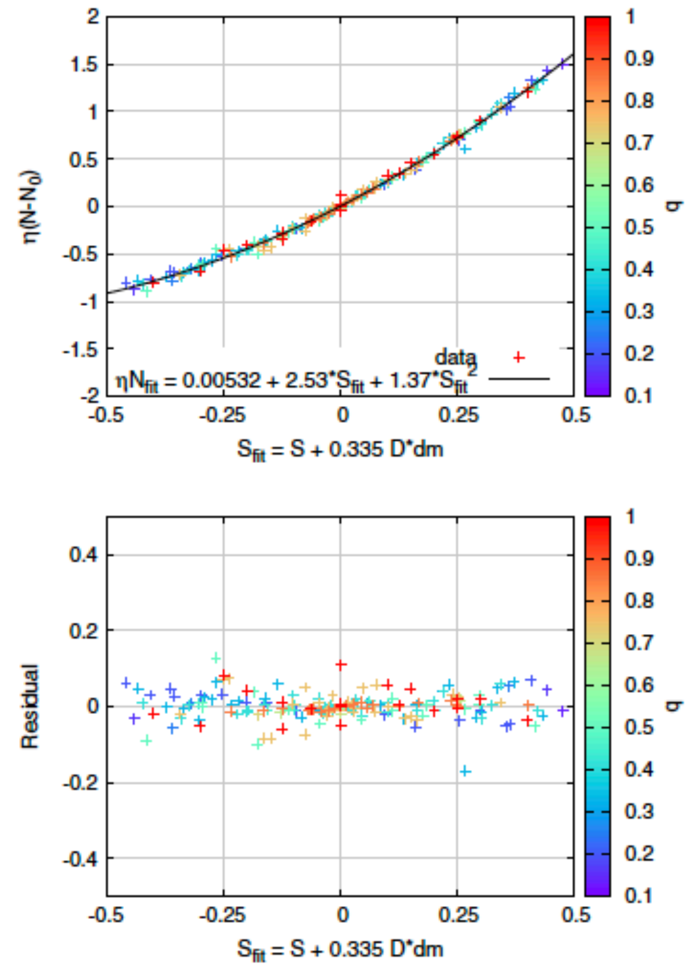

FIG. 2. The difference in number of orbits with respect to the nonspinning case for full numerical binary black hole mergers. We use the (2,2) mode of the waveform and calculate the number of cycles between $m\omega = 0.07$ and $m\omega_{\rm peak}$. We study in detail the cases with $q = 1.00$, $q = 0.85$, $q = 0.75$, $q = 0.4142$, $q = 0.50$, $q = 0.333$ and $q = 0.20$ and fit a quadratic dependence with the spin variables to extract the linear spin coefficients of $\vec{S}\cdot\hat{L} + C\delta m\vec{\Delta}\cdot\hat{L}$. The residuals of such a fit are also displayed showing no systematics.

GW150914: Remnant properties

we find

$$0.039 < E_{rad}/m < 0.053$$
$$0.578 < \chi_f < 0.753$$
$$0 < V_{recoil} < 492[\mathrm{km/s}]$$

Comparing these ranges to the GW150914 properties paper [4] (and converting from total mass and final mass to energy radiated and propagating the errors appropriately)

$$0.041 < E_{rad}/m < 0.049$$
$$0.60 < \chi_f < 0.72$$

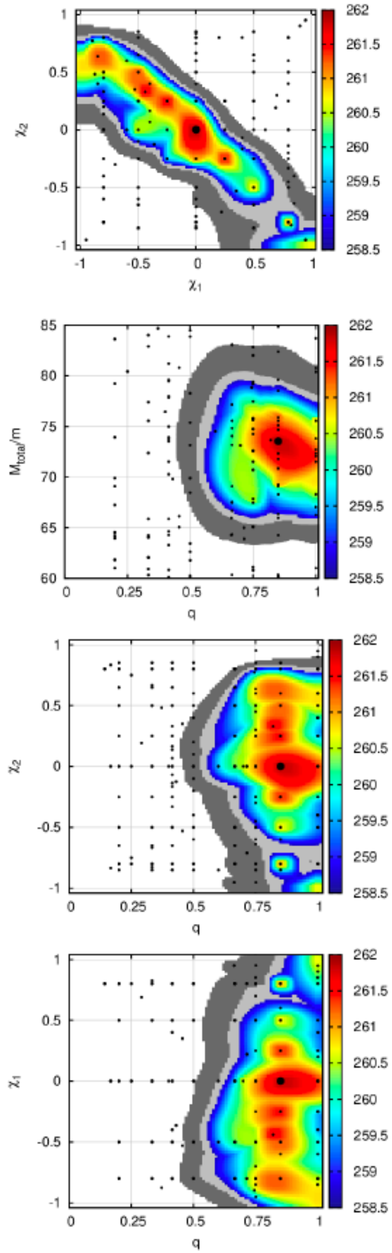

FIG. 5. 90% confidence interval heat maps of the GW150914 likelihood for the aligned binary mass ratio and individual spin parameters. The dark grey region constitutes the 99.7% (3σ) confidence interval range, and the light grey is the 95% (2σ) range. The colored region shows the $\ln \mathcal{L}$ of the values within the 90% confidence interval. The black points indicate the placement of the numerical simulations.

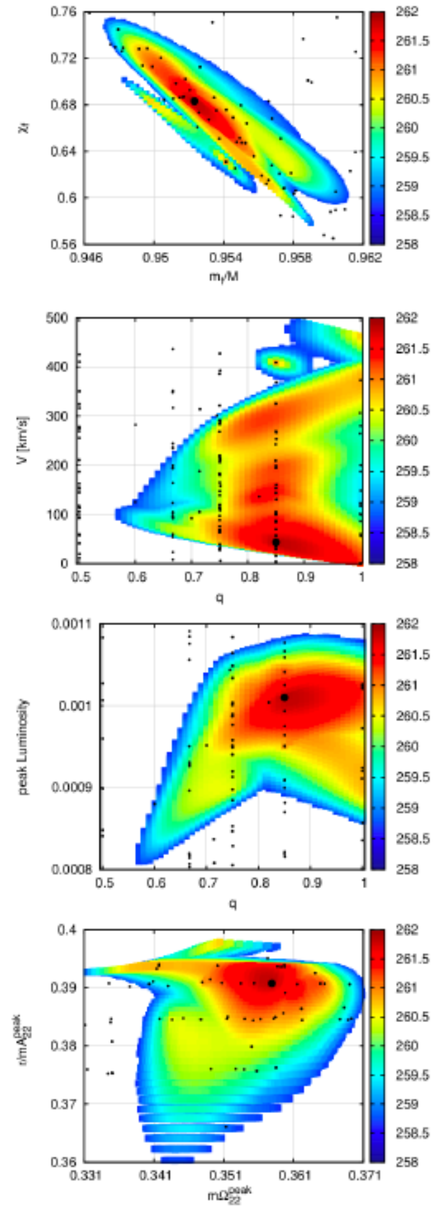

FIG. 7. Final parameter space heatmaps for simulations that fall within the 90% confidence interval for the final mass, spin, recoil, peak luminosity, and orbital frequency and strain amplitude at peak strain. A maximum $\ln \mathcal{L}$ is reached for $m_f/m = 0.952$, $\chi_f = 0.683$, $V = 44$ km/s, $L^{peak} = 1.01e-3$, $m\Omega_{22}^{peak} = 0.358$, and $(r/m)A_{22}^{peak} = 0.391$.

GW150914: Precession

- Nearly 200 simulations
- One hole spinning,
- All orientations
  (q>1 is the smaller one)
- $\frac{s}{m^2} = 0.8$

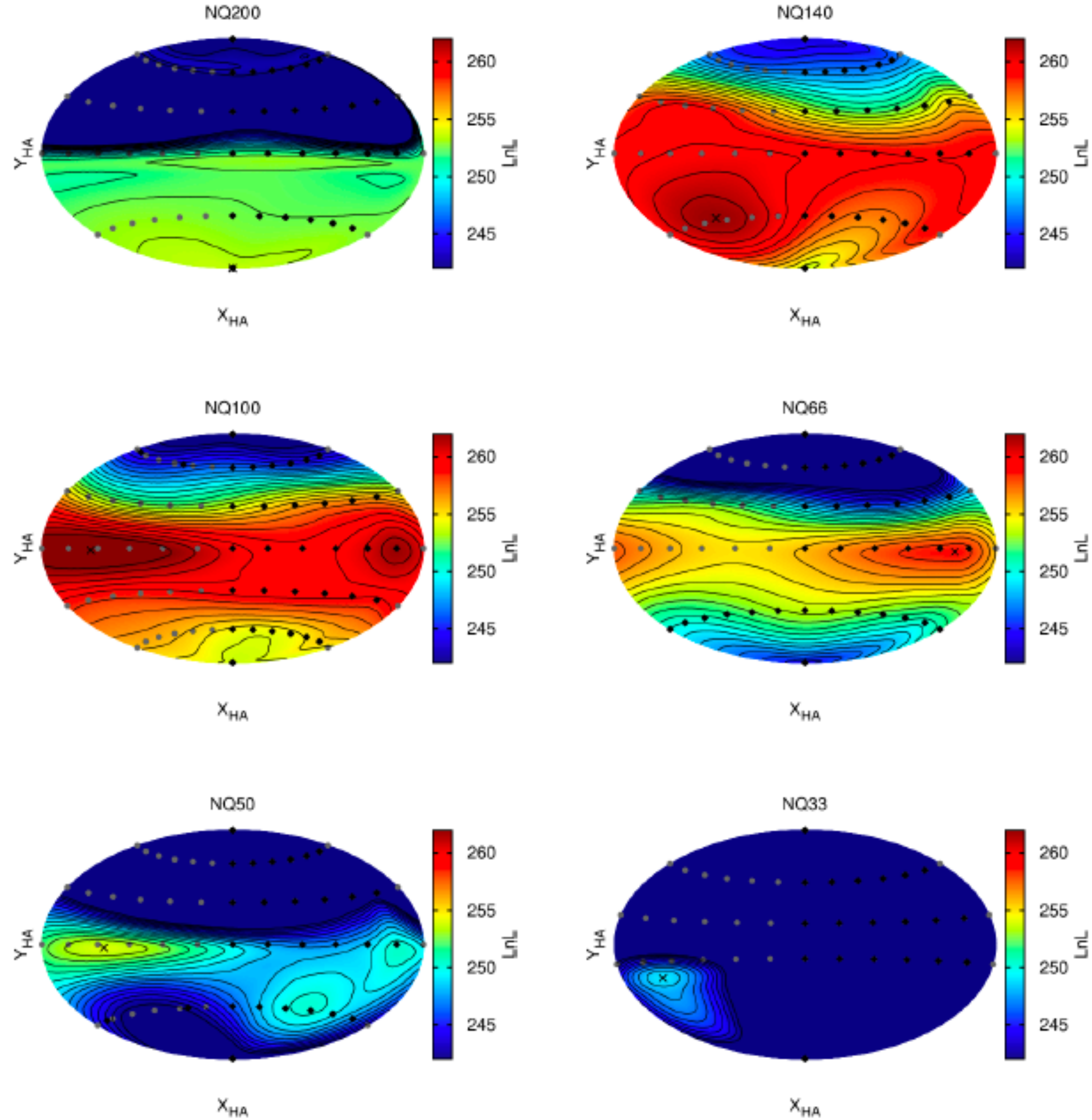

FIG. 8. Heat maps of the GW150914 likelihood for each of the six mass ratio panels covering form $q = 2$ to $q = 1/3$ (labeled from NQ200 to NQ33 respectively) and large black hole spin oriented over the sphere (interpolated using multiquadric radial basis functions between simulations). The individual panel with $q = 1$ contains the highest likelihood (near the orbital plane orientation), and it is bracketed by the $q = 1.4$ and $q = 0.66$ panels ($q > 1$ here means the smaller black hole is the one spinning). We have used Hammer-Aitoff coordinates X_{HA}, Y_{HA}, to represent the map and level curves. The interpolated $\ln \mathcal{L}$ maximum location is denoted by the an x in the plots, the black points are simulations, and the gray points are extrapolated simulations using the sinusoidal dependence of the azimuthal angle.

GW150914: Extrinsic parameters and waveforms

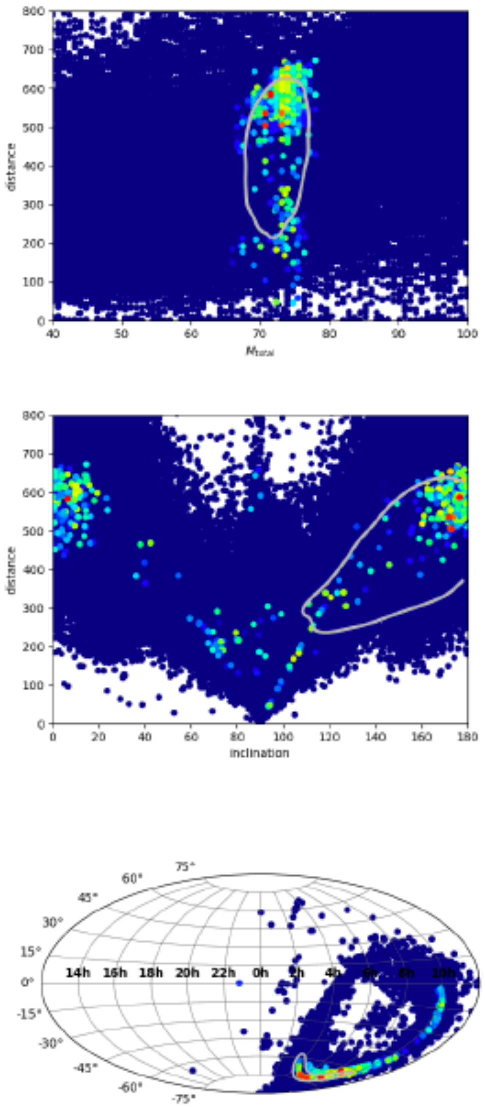

FIG. 9. We use the results of the Monte-Carlo intrinsic log-likelihood calculations (100 samples in M_{total} for each simulation in the catalog) to estimate the extrinsic parameters of GW150914. The gray boundary denotes the public LIGO GWTC-1 data and the colored points indicate simulations which fell within the $\ln \mathcal{L} > \max \ln \mathcal{L} - 3.125$, or roughly the 90% confidence interval. The dark blue background points denote simulations outside of the 90% confidence interval.

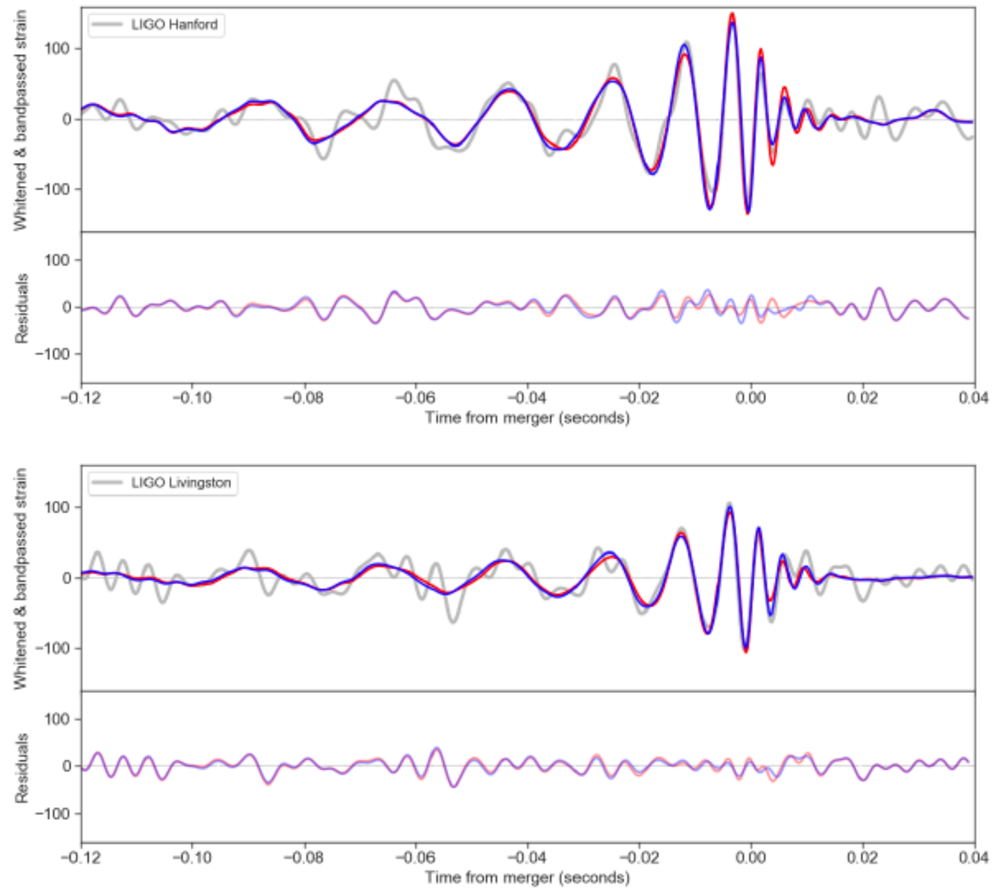

FIG. 10. Direct comparison of the highest $\ln \mathcal{L}$ nonprecessing simulation (RIT:BBH:0113 in red) and precessing simulation (RIT:BBH:0126 in blue) to the Hanford (top) and Livingston (bottom) GW150914 signals. The bottom panel in each figure shows the residual between the whitened NR waveform and detector signal.

TABLE I. Highest $\ln \mathcal{L}$ nonprecessing and precessing simulations. The nonprecessing simulation has highest overall $\ln \mathcal{L}$, and the precessing simulation has 13th highest.

Config.	q	$\vec{\chi}_1$	$\vec{\chi}_2$	$\vec{S}_{hu}/m^2$	$M_{total}/M_\odot$	$\ln \mathcal{L}$
RIT:BBH:0113	0.85	(0, 0, 0)	(0, 0, 0)	(0, 0, 0)	73.6	261.8
RIT:BBH:0126	0.75	(-0.46, -0.48, -0.44)	(0.06, -0.38, 0.12)	(-0.15, -0.42, -0.11)	72.5	260.5

Bonus: GW170104

This approach had already proven very successful when applied to GW170104*.

(It required an homogeneous set of simulations since the differences in LnL are subtle).

*J. Healy et al., Phys. Rev. D97, 064027 (2018)

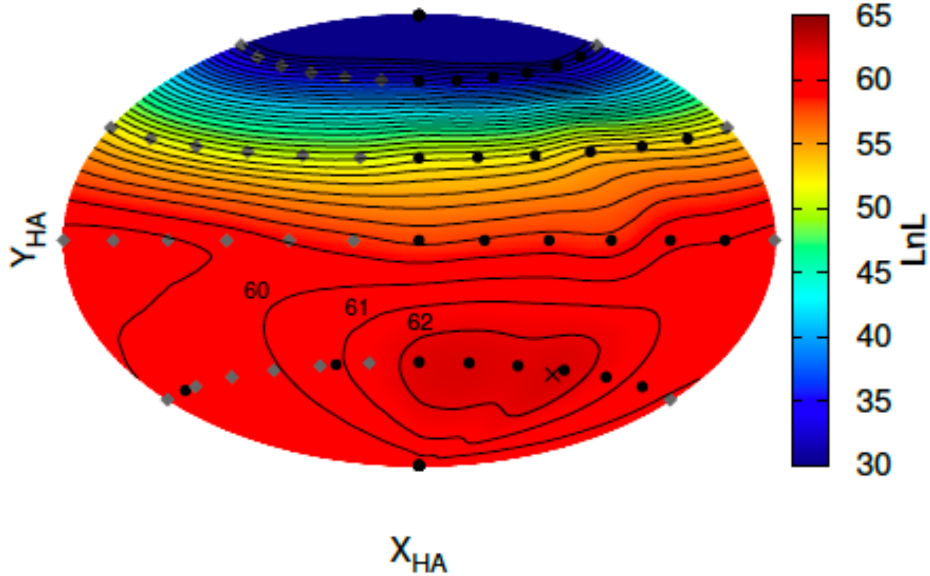

FIG. 8. The log-likelihood of the NQ50THPHI series [101] as a color map with red giving the highest $\ln \mathcal{L}$ and blue the lowest. The black dots (and grey diamonds, obtained by symmetry) represent the NR simulations and we have used Hammer-Aitoff coordinates X_{HA}, Y_{HA}, to represent the map and level curves with the top values of $\ln \mathcal{L} = 60, 61, 62$. The maximum, marked with an X, is located at TH=137, PH=87 reaching $\ln \mathcal{L} = 62.6$.

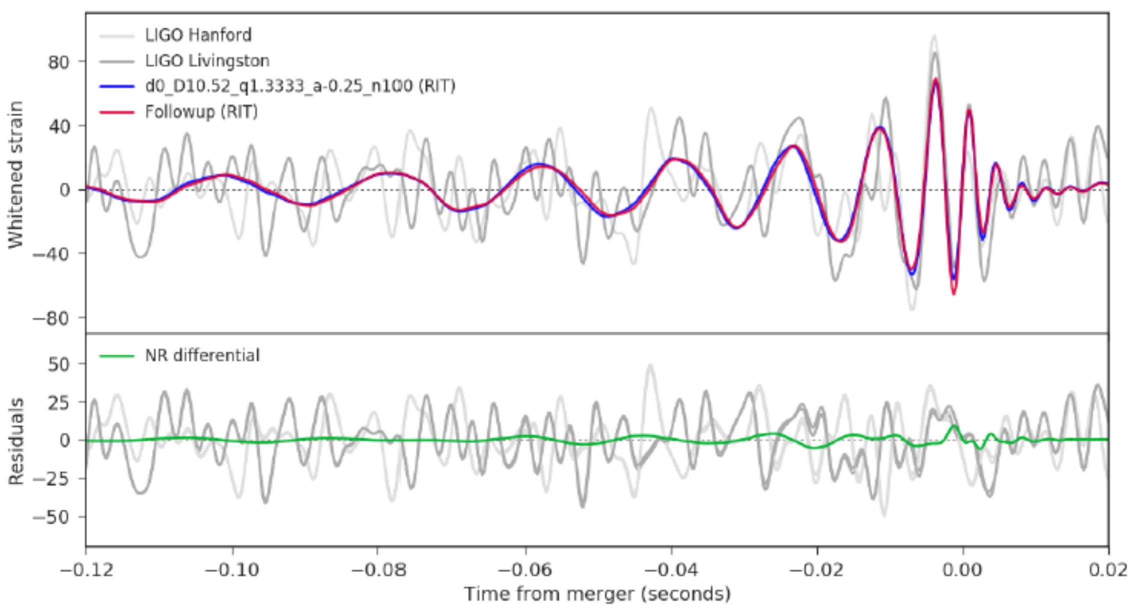

Discussion

- ✓ We have developed a complete and independent method to analyze GW signals from BBH with NR solutions to GR (Without resourcing to phenomenology)
- ✓ Applied to O1/O2, and for O3+:
- ○ Interesting sources to detect yet
  - ➢ Very highly spinning BHs (s > 0.9)
  - ➢ Not comparable BBH mass ratios (q < 1/5-1/10)
  - ➢ BH-NS systems (q ~ 1/7– 1/20)
- ❖ RIT Catalog3: Complete single spinning q's; Complete aligned spins 0.95; down to q -> 1/15.
- ❖ A collection of NR catalogs (RIT+SXS+GT+BAM+) can be used for even better coverage.

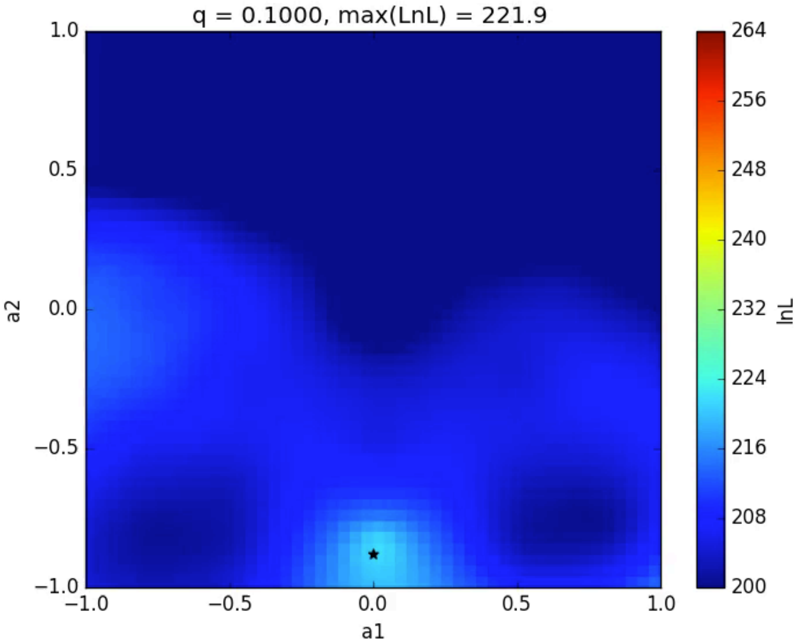

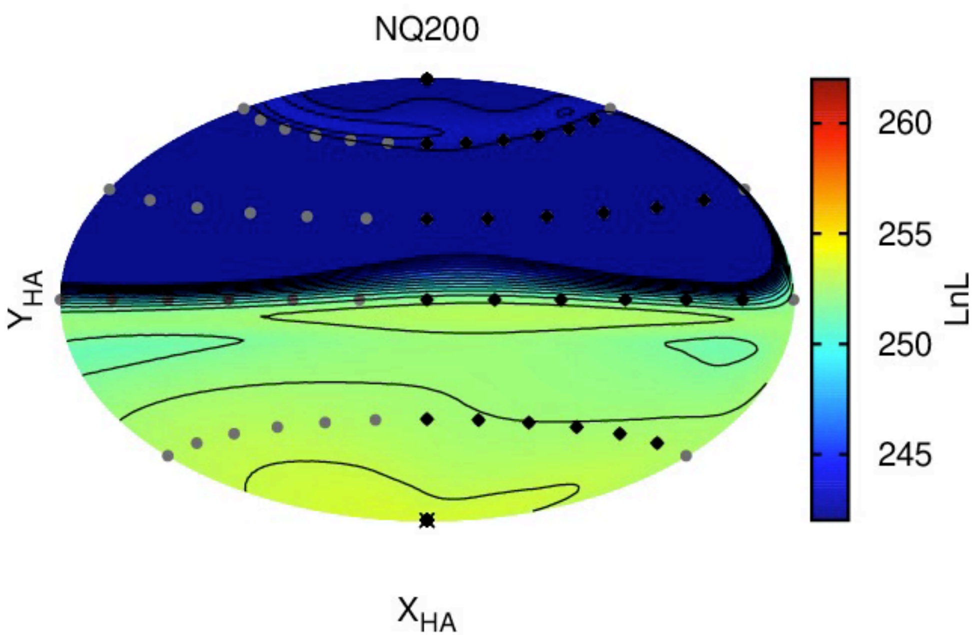

Extra

Discussion: Observational effects

The leading flip-flop period is now given by

$$T_{ff} \approx 2,000\, yr\, \frac{(1+q)}{(1-q)} \left(\frac{r}{1000M}\right)^{5/2} \left(\frac{M}{10^8 M_\odot}\right).$$

which is much shorter than the gravitational radiation

$$T_{GW} \approx 1.22\, 10^6\, yr \left(\frac{r}{1000M}\right)^4 \left(\frac{M}{10^8 M_\odot}\right),$$

alignment processes can be less effective than expected when the flip-flop of spins is taken into account.

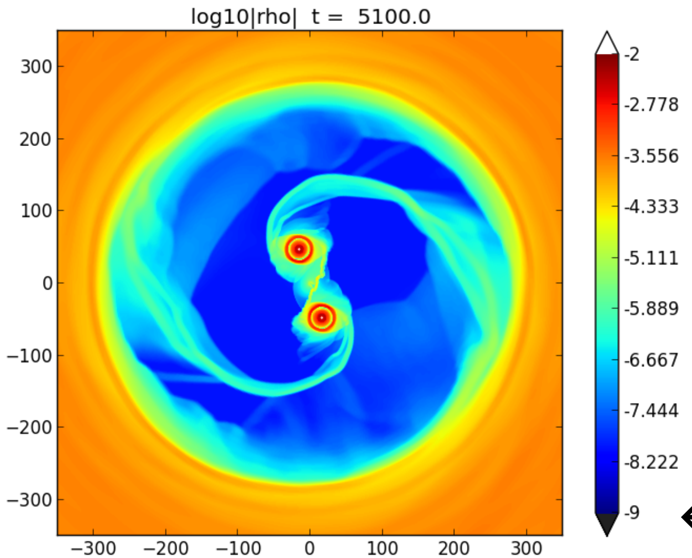

← Simulation by RIT group

Accretion disk internal rim will change location with spin orientation. This changes

- Efficiency of the EM radiation
- Spectrum of EM radiation (hard part)
- Cutting frequency of oscillations

Proper modeling using GRMHD simulations

X-shaped galaxies should show 'orange peeling' jets when they were about to merge

- For our simulation this corresponds to 1.2 seconds for 10Msun and 142 days for 10^8Msun

- The effect is still present in unequal mass binaries, (and BH-NS and NS-NS) with smaller flip-flop angles.

We need full numerical GRMHD simulations

Flip-flop instability

2 PN Analytic study

$$d^2(\vec{S}_i \cdot \hat{L})/dt^2 = -\Omega_{ff}^2\, \vec{S}_i \cdot \hat{L} + \cdots$$

$$\begin{aligned}\Omega_{ff}^2 =\; & \frac{9}{4}\frac{(1-q)^2 M^3}{(1+q)^2 r^5} + 9\,\frac{(1-q)\,(S_{1\hat{L}} - S_{2\hat{L}})M^{3/2}}{(1+q)r^{11/2}} \\ & - \frac{9}{4}\frac{(1-q)\,(3+5\,q)\,{S_{1\hat{L}}}^2}{q^2 r^6} + \frac{9}{2}\frac{(1-q)^2\, S_{1\hat{L}}\, S_{2\hat{L}}}{q r^6} \\ & + \frac{9}{4}\frac{(1-q)\,(5+3\,q)\,{S_{2\hat{L}}}^2}{r^6} + \frac{9}{4}\frac{S_0^2}{r^6} + 9\,\frac{(1-q)^2\, M^4}{(1+q)^2\, r^6},\end{aligned} \tag{1}$$

where $\vec{S}_0/M^2 = (1+q)\left[\vec{S}_1/q + \vec{S}_2\right]$.

$$\Omega_{ff}(q, \vec{\alpha}_1, \vec{\alpha}_2, R_c) = 0. \tag{2}$$

The solution of this quadratic equation for antialigned spins leads to two roots $R_c^{\pm}$.

$$R_c^{\pm} = 2M\,\frac{A \pm 2(\alpha_{2L} - q^2\alpha_{1L})\sqrt{B}}{(1-q^2)^2}, \tag{3}$$

$$\begin{aligned} A &= (1+q^2)(\alpha_{2L}^2 + q^2\alpha_{1L}^2), \\ &\quad -2q(1+4q+q^2)\alpha_{1L}\alpha_{2L} - 2(1-q^2)^2 \\ B &= 2(1+q)\left[(1-q)q^2\alpha_{1L}^2 - (1-q)\alpha_{2L}^2\right. \\ &\quad \left. -2q(1+q)\alpha_{1L}\alpha_{2L} - 2(1-q)^2(1+q)\right].\end{aligned}$$

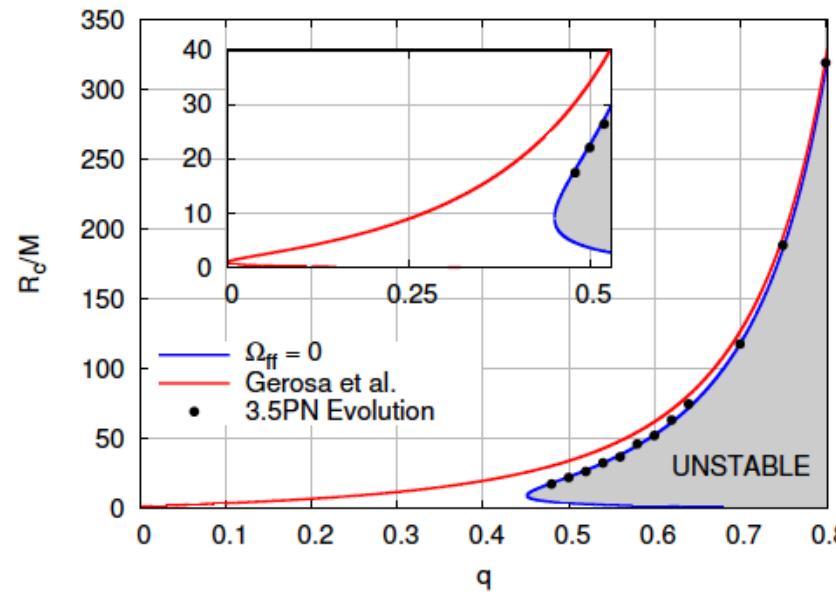

FIG. 3. The instability region, between $R_c^{\pm}$, as a function of the mass ratio, q, as the binary transitions from real to imaginary flip-flop frequencies (blue curve) for maximal spins $\alpha_{1L} = -1$ and $\alpha_{2L} = +1$. For comparison also plotted are $r_{ud\pm}$ from [8] (red curve). The dots correspond to 3.5PN evolutions.

From: C.O.Lousto & J.Healy, Phys. Rev., **D93**, 124074 (2016)

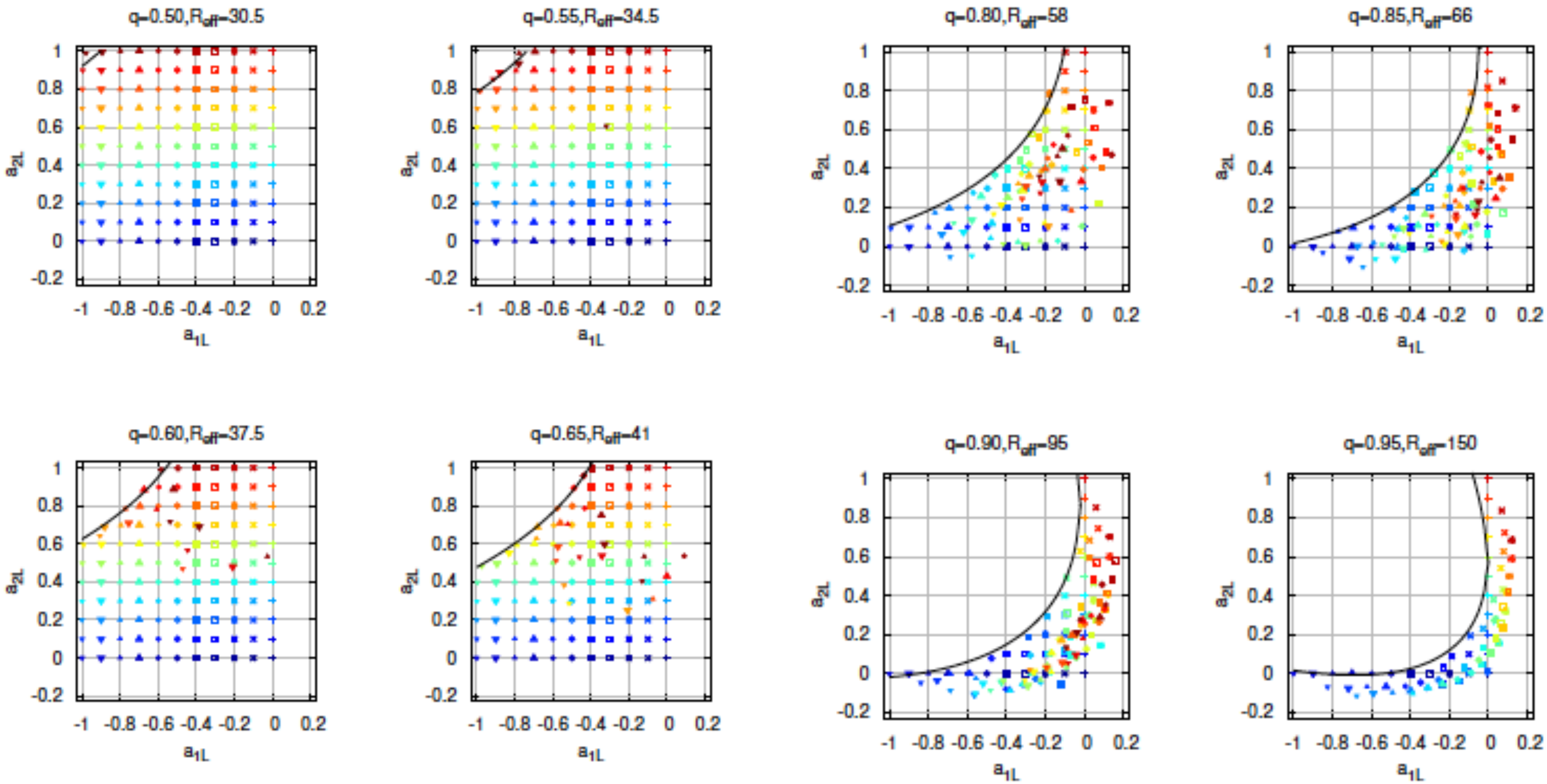

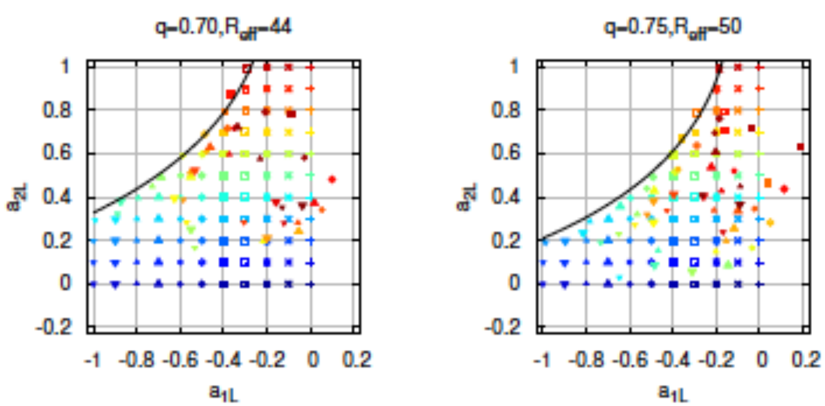

FIG. 1. Snapshots of the spin components along the orbital angular momentum at a binary separation $r/M = 11$. The integration of the PN evolution equations for each binary mass ratio q, started at $r/M > R_c$ with a uniform distribution of spins in the range $0 \leq \alpha_{2L} \leq 1$ for the large BH and $-1 \leq \alpha_{1L} \leq 0$ for the small BH, which was antialigned with the orbital angular momentum by 179-degrees. The color indicates the original value of the spins. The black curve models the depopulation region as given in Eq. (4).

Beaconing binaries

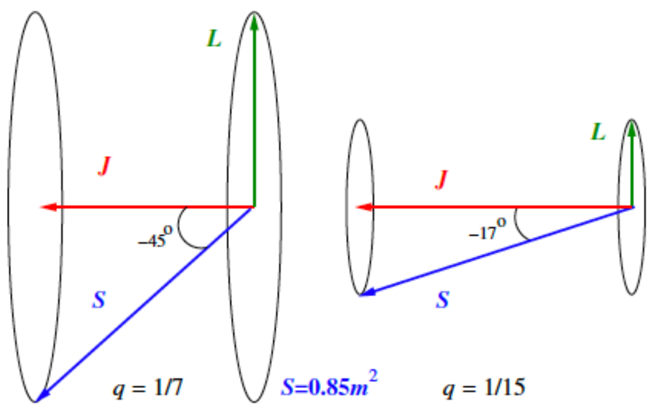

FIG. 1. Initial configuration of the orbital angular momentum $\vec{L}$, large hole spin $\vec{S}$, and total momentum of the system, $\vec{J}$. Both the spin and the orbital angular momentum precess (counter-clockwise) around $\vec{J}$ as the system evolves.

In order to qualitatively understand the basic dependence of the beaconing phenomena on the binary parameters, we use a low order post-Newtonian analysis [see Eq. (3.2c) of Ref. [42]] with $\vec{S}_2 \cdot \hat{L} = -\vec{L} \cdot \hat{L}$ initially, to find a frequency of precession of $\vec{L}$:

$$M\Omega_L = 2\alpha_2^J/(1+q)^2(M/r)^3, \tag{1}$$

where r is the coordinate separation of the holes, $\alpha_2^J = \vec{S}_2 \cdot \hat{J}/m_2^2$ the dimensionless spin of the large hole along $\vec{J}$ (perpendicular to $\vec{L}$), $M = m_1 + m_2$ the total mass of the system, and $q = m_1/m_2 \leq 1$ its mass ratio.

The critical separation radius r_c, characterizing the middle of the transitional precession, where the condition $S_2^L = \vec{S}_2 \cdot \hat{L} = -\vec{L} \cdot \hat{L} = -L$ is met is hence

$$(r_c/M)^{1/2} = (\alpha_2^L/2q)\left(1 + \sqrt{1 - 8(q/\alpha_2^L)^2}\right).$$

This configurations leads to an L-flip

$q > 1/4$ for $r_c > 10M$

GW Beaconing and Polarization effects

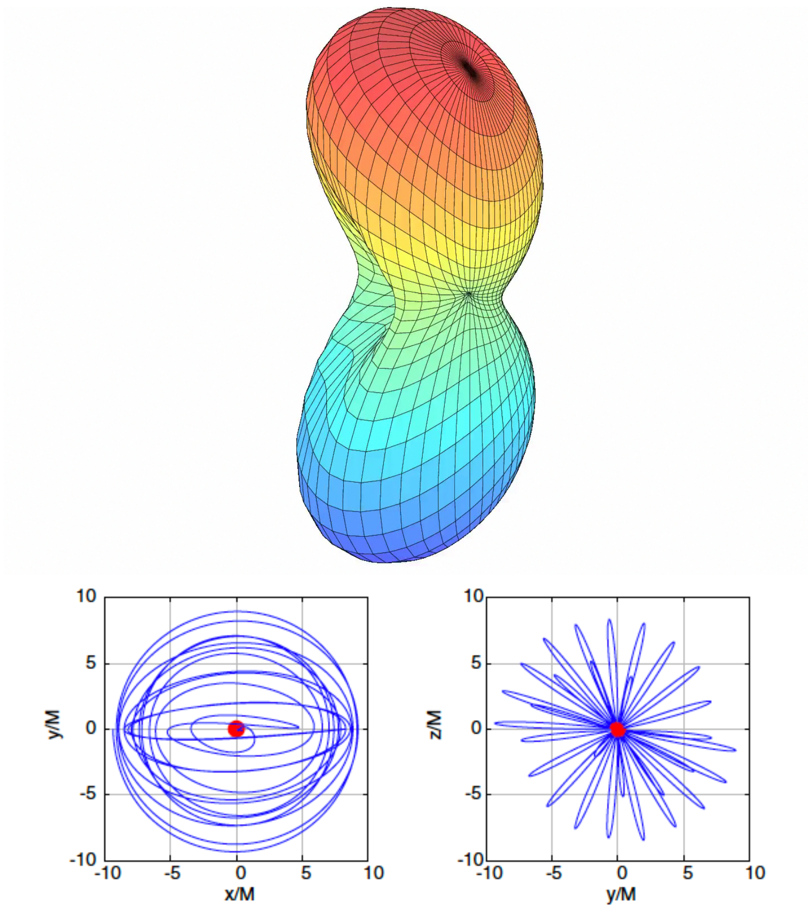

FIG. 5. The beaconing effect displayed by the power radiated for the binary case with mass ratio $q = 1/15$ as seen from the z axis (the initial direction of the orbital angular momentum) (above) and (below) the detail of the black hole trajectories in the initial orbital plane (left) and seen from an observer along the x axis (right).

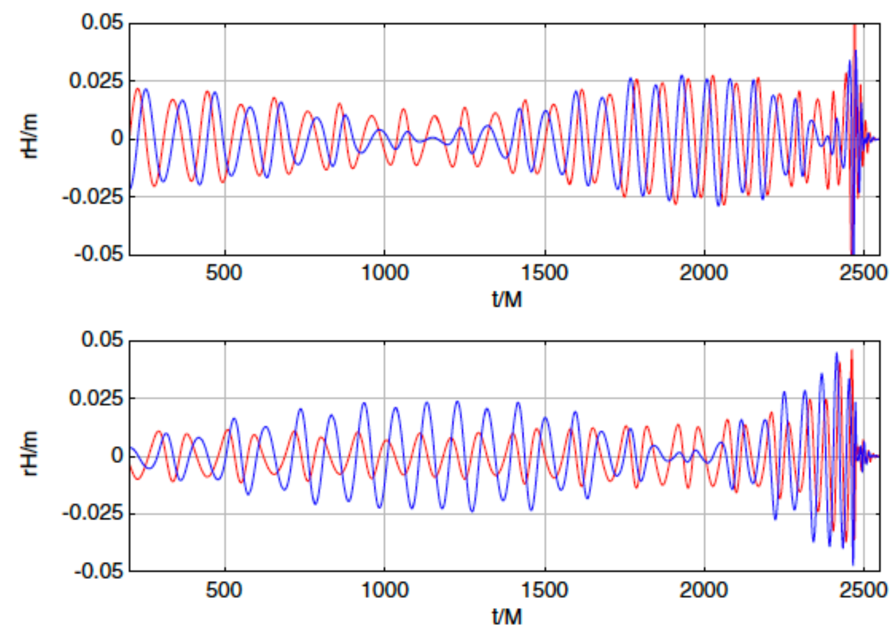

FIG. 4. The two polarizations of the waveform strain of the system with mass ratio $q = 1/15$ as seen from the z axis (the initial direction of the orbital angular momentum) (above) and the same waveform strain as seen from the y axis (below) reconstructed using modes up to $l_{\max} = 5$.

GW Beaconing and Polarization effects

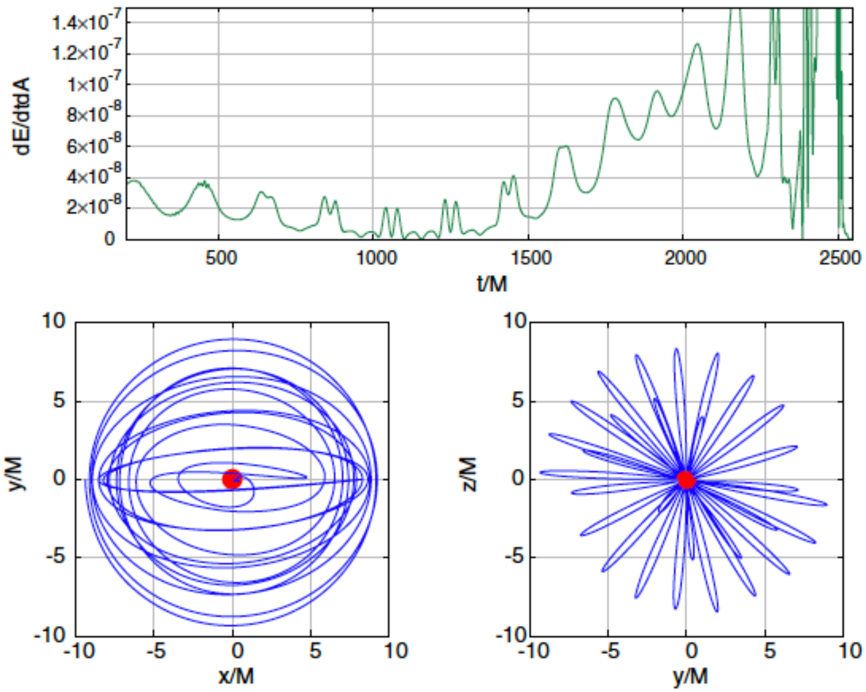

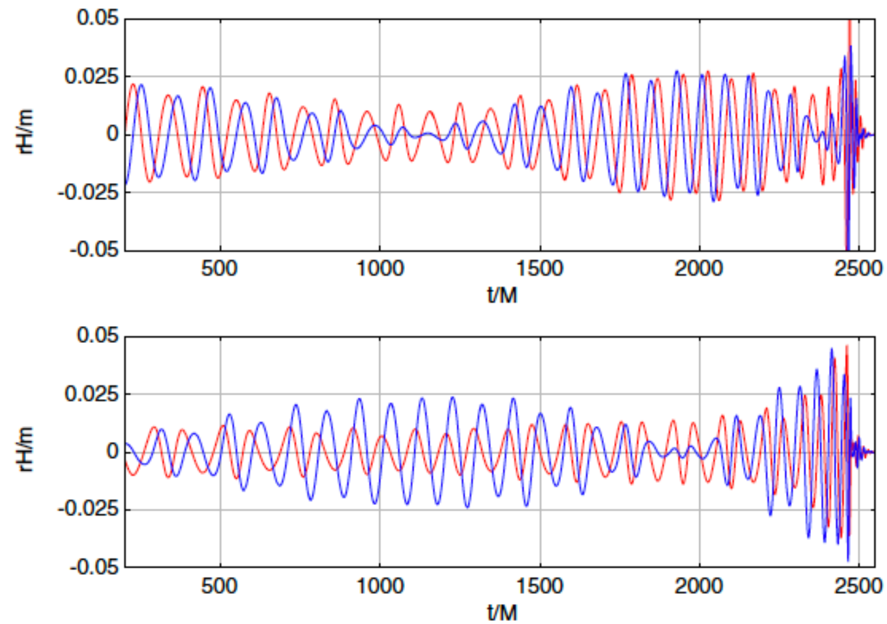

FIG. 5. The beaconing effect displayed by the power radiated for the binary case with mass ratio $q = 1/15$ as seen from the z axis (the initial direction of the orbital angular momentum) (above) and (below) the detail of the black hole trajectories in the initial orbital plane (left) and seen from an observer along the x axis (right).

FIG. 4. The two polarizations of the waveform strain of the system with mass ratio $q = 1/15$ as seen from the z axis (the initial direction of the orbital angular momentum) (above) and the same waveform strain as seen from the y axis (below) reconstructed using modes up to $l_{\max} = 5$.

Observational consequences

- Beaconing effect likely for $q < 1/4$ and retrograde BBH systems
- Beaconing effect leads to higher chances of seeing a system face-on
- GW polarizations look like pretty different
  - Important to measure them
  - Relevant for LIGO, LISA and PTA merger observations

- When matter present, EM counterparts may have characteristic features on the beaconing frequency scale

➢ RIT GRMHD Simulation